Monthly Notices
of the
ROYAL ASTRONOMICAL SOCIETY

Mon. Not. R. Astron. Soc. **422,** 420–433 (2012) doi:10.1111/j.1365-2966.2012.20624.x

Energy deposition by weakly interacting massive particles: a comprehensive study

C. Evoli,[1,2]★ M. Valdés,[2,3] A. Ferrara[2] and N. Yoshida[3]

[1]*National Astronomical Observatories, Chinese Academy of Sciences, Beijing 100012, China*
[2]*Scuola Normale Superiore, Piazza dei Cavalieri 7, 56126 Pisa, Italy*
[3]*IPMU, University of Tokyo, 5-1-5 Kashiwanoha, Kashiwa, Chiba 277-8568, Japan*

Accepted 2012 January 22. Received 2012 January 22; in original form 2011 July 25

ABSTRACT

We present results obtained with the updated version of our code MEDEA2, which includes all physical processes necessary to study the energy deposition in the surrounding environment from primary photons and fast leptons produced by dark matter (DM) particle decay/annihilation. Such interactions now include also Compton scattering of primary photons off electrons and pair creation of photons on atoms. Our ultimate aim is a thorough study of the impact of DM annihilations on the thermal and ionization history of the high-redshift intergalactic medium (IGM) during the dark ages. In addition, a precise determination of the effects of DM decays/annihilations can help constrain its nature. We present the results for some selected DM candidates: (i) a 10-GeV bino-like neutralino; (ii) a heavy DM candidate of rest mass 1 TeV that pair annihilates into muons; and (iii) a 200-GeV wino-like neutralino with a pair annihilation into W^+W^- pairs. An interface to DARKSUSY allows us to use the computed annihilation spectra in input for our code and follow the complete secondary cascade. The fractional energy depositions into the IGM depend strongly on the DM particle rest mass: whereas for the 10-GeV particle the absorbed energy fraction, in the redshift range $10 < z < 1000$, is $\gtrsim$50 per cent, higher mass candidates deposit their energy less efficiently ($\sim$1–10 per cent), making their impact on the high-z IGM considerably weaker. Noticeably, our approach allows us to consistently follow the low-energy deposition of the cascade products, which can be of interest for a broad range of applications. Finally, we provide both tabulated results and analytical fits that can be readily implemented in theoretical studies of the effects and detectability of the most popular DM candidates.

Key words: intergalactic medium – cosmology: theory – dark matter – diffuse radiation.

1 INTRODUCTION

According to the widely accepted Λ cold dark matter (ΛCDM) cosmology theory, the Universe is made mostly of *dark* components: dominant over the 4 per cent baryons are the 75 per cent of dark energy and 20 per cent of dark matter (DM; see e.g. Komatsu et al. 2009). The nature of these components is elusive and far from understood and is a crucial issue in cosmology.

Although a clear detection has not been achieved yet, an impressive amount of indirect proofs of the existence of DM has been collected in the past decades. According to our understanding of the evolution of the Universe, cold dark matter (CDM) is in fact needed to explain a large number of observations both at galactic scale, such as the large velocity dispersion of the members of galaxy clusters and the galactic rotation curves, and at cosmological scale, where cosmic microwave background (CMB) power spectrum data are compatible with a DM component yielding almost one-quarter of the total cosmic energy budget today. Moreover, its existence seems also necessary to explain structure formation in the Universe since gravity acting on baryons alone could not amplify the tiny density fluctuations which we measure in the CMB anisotropies to form the large-scale structure that we witness today.

Among the most popular DM candidates are weakly interacting massive particles (WIMPs), particles with masses near the electroweak (EW) scale whose existence and properties are predicted by several extensions of the standard model of particle physics. Supersymmetry (SUSY), which has been built on the success of the EW physics, in particular could offer the framework in which DM particles arise naturally. The minimal supersymmetric extension of the standard model (MSSM) provides many testable predictions at collider experiments (Nath et al. 2010), and the lightest SUSY

★E-mail: carmelo.evoli@me.com

particle (LSP) is in fact stable and can only be destroyed via pair annihilation, making it an excellent DM candidate (Goldberg 1983; Ellis et al. 1984). The nature of the LSP in a specific supersymmetry model depends on how supersymmetry is broken. Among the LSP candidates some have been observationally ruled out (e.g. the sneutrino), while others are increasingly popular among the scientific community, such as the lightest neutralino.

Neutralinos – like any WIMP candidate – have a small but measurable interaction cross-section with ordinary matter; therefore, they can in principle be directly detected by ground-based experiments. In recent years several direct detection experiments have found anomalies possibly compatible with a DM signal: DAMA and DAMA/LIBRA (Bernabei et al. 2008) detected an annual modulation in the total event rate consistent with the effect expected from WIMP elastic scatterings; CDMS (CDMS II Collaboration 2010) reported two events in the signal region and CoGeNT (Aalseth et al. 2011a) found a low-energy exponential tail in their count rate, consistent with the shape predicted for the signal from a WIMP in a narrow range of masses, namely a few GeV. More recently, CoGeNT collaboration has reported new results based on 145 kg d of data showing an excess of events at low recoil energies with a 2.8σ statistically significant detection of annual modulation (Aalseth et al. 2011b).

Such approach has not brought conclusive results (see e.g. Fitzpatrick, Hooper & Zurek 2010; Kopp, Schwetz & Zupan 2010; Savage et al. 2011), and in the past few years the detection of the secondary particles resulting from hypothetical WIMP annihilations in regions where DM density is very high (such as in the centre of the Milky Way) became popular as a tool to indirectly probe the nature of DM. Recent observation of the electron/positron spectrum in the cosmic ray energy spectrum data from the *Payload for Antimatter Matter Exploration and Light-nuclei Astrophysics* (*PAMELA*), *Advanced Thin Ionization Calorimeter* (*ATIC*), *Fermi* Large Area Telescope (*Fermi*-LAT) and HESS experiments has been explained by some groups as a trace of annihilating DM with mass between 1 and 2 TeV (e.g. Bergström et al. 2009; Cirelli et al. 2009a). However, a careful analysis of the *Fermi*-LAT data toned down the early enthusiasm and put particularly strong constrains on the annihilation of the most popular DM candidates, such as the lightest neutralino of supersymmetric models (Abdo et al. 2010c).

Another clean test of the nature of DM will come in the near future from the opening of a new observational window in the redshifted H I 21-cm hyperfine triplet–singlet line from redshifts $z > 6$ that will allow direct detection of neutral hydrogen during the so-called dark ages (see e.g. Kassim et al. 2004; Bowman, Morales & Hewitt 2005; Peterson, Pen & Wu 2005; Wyithe, Loeb & Barnes 2005).

Several authors in fact showed in recent years that DM, by annihilating or decaying and therefore by injecting energy into the IGM, can change the ionization and thermal history of the mostly uniform gas during the dark ages down to the epoch of reionization (Chen & Kamionkowski 2004; Mapelli, Ferrara & Pierpaoli 2006; Cirelli, Iocco & Panci 2009b). Such effects can in turn produce deviations in the all-sky behaviour of the H I 21-cm line of up to ∼30 mK depending on the DM candidate; such signal, if observed, would be an indirect signature of the nature of DM (see e.g. Furlanetto, Oh & Pierpaoli 2006; Shchekinov & Vasiliev 2007; Valdés et al. 2007; Natarajan & Schwarz 2009). The results that we present in this paper constitute the necessary ingredients for an extension of such studies to DM candidates with rest mass of the order of 10 GeV to 1 TeV, which have been recently favoured by observations.

The facilities that will observe the high-redshift H I and potentially constrain the nature of DM are large radio interferometers either planned or currently in construction such as the Low frequency Array (LOFAR[1]), the 21 Centimetre Array (21CMA[2]), the Murchison Widefield Array (MWA[3]) and the Square Kilometre Array (SKA[4]).

The aforementioned observations of the hypothetical impact of DM decays/annihilations on the surrounding gas require a precise calculation of the amount of energy that can be transferred from the decay/annihilation products to the IGM, i.e. it is necessary to address the issue of following the complex secondary energy cascade from the energetic primary photons, electrons and positrons that arise in many models of decaying/annihilating DM.

In Valdés & Ferrara (2008, hereafter VF08) and Valdés, Evoli & Ferrara (2010) (hereafter VEF10), we have studied the particle cascades generated by a single primary electron into the IGM (see also Shull 1979; Shull & van Steenberg 1985; Furlanetto & Stoever 2010). To this aim, we have developed a new code, called MEDEA (Monte Carlo Energy Deposition Analysis), which includes bremsstrahlung and inverse-Compton (IC) processes, along with H/He collisional ionizations and excitations, and electron–electron collisions. With this code, we were able to compute the energy partition into heating, excitations and ionizations as a function of the electron initial energy, the ionization fraction and the redshift.

In this paper we aim to consider the energy depositions induced by the annihilation products of specific DM models. In the context of the IGM, the only particles produced by DM annihilation that can have relevant interactions with the medium are electrons, positrons and photons. In fact, weak and hadronic cross-sections are small enough that neutrinos and baryons produced after recombination interactions with the medium can be safely neglected (Chen & Kamionkowski 2004).

To this aim, we present here an updated version of our code, MEDEA2, capable of precisely following the secondary products from an initial distribution of electrons, positrons and photons with different energies. With respect to the previous version of the code, we have implemented all the relevant interactions of positrons and photons with the environment and we have optimized the treatment of IC scattering.

These improvements make the code suitable for studying DM energy depositions: in fact, we provide an interface to DARKSUSY that allows us to use the annihilation spectra obtained from this code to calculate the initial particle distributions for some of the most popular DM models. DARKSUSY (Gondolo et al. 2004) is a publicly available advanced numerical package for neutralino DM calculations that allows us, among the other things, to obtain the spectrum of standard model particles in the MSSM framework for a DM candidate defined by its mass and the dominant annihilation channel. It has been recently pointed out (Ciafaloni et al. 2011) that such calculation is not accurate for very heavy WIMPs because these kind of codes do not include the radiative emission of soft EW gauge bosons. To discuss the heavy WIMP regime, we will consider the lepton/photon yields as computed in Ciafaloni et al. (2011) including EW corrections.

Note that the calculation of the energy deposition of DM annihilation products on high-redshift IGM is just one specific application

[1] http://www.lofar.org/
[2] http://21cma.bao.ac.cn/
[3] http://www.mwatelescope.org/
[4] http://www.skatelescope.org/

of a code which is very versatile and allows us to calculate the final secondary products from any distribution of primary photons and leptons with energies below a few TeV: MEDEA2 can therefore represent a precious tool for the study of a very large number of astrophysical systems.

A similar calculation has been performed by Ripamonti, Mapelli & Ferrara (2007) and Slatyer, Padmanabhan & Finkbeiner (2009) and used to calculate the perturbations to the ionization history induced by different DM candidates and the integrated impact on the CMB temperature and polarization angular power spectra. However, in these works the evolution of the initial spectra is followed analytically [in Ripamonti et al. (2007), only a monoenergetic spectra has been considered, whereas in Slatyer et al. (2009) the calculations has been extended for arbitrary spectra of the DM annihilation products and for DM masses up to TeV scales].

Our approach is instead based on a Monte Carlo algorithm that relies on repeated random sampling of the relevant physical quantities and processes, in our case cross-sections and interaction probabilities. This allows us to follow numerically the complex evolution of the physical system considered, i.e. the energy injection from electrons, positrons and photons into the IGM keeping track of all the individual particles.

The rest of the paper is organized as follows. In Section 2 we introduce the latest observational constraints for DM and make a choice of the best candidates to study in detail. In Section 3 we describe the considered physical process and their implementation into our code MEDEA2, which is a major overhaul and extension of our code MEDEA described in VEF10. In Section 4 we present the results and analyse their dependence on the parameter choices. Section 5 is dedicated to the discussions and implications of our results.

2 DARK MATTER MODELS

In this section we first introduce some of the most recent observational constrains of the nature of DM and accordingly we make a choice of three among the promising annihilating DM candidates for our study. Using these sets of particle parameters as a starting point, we will be able to perform a detailed numerical calculation of the secondary cascade that arises from the photon and lepton distributions generated by the DM annihilations. To do so, we use our improved code MEDEA2, using as input the photon, electron, positron energy distributions calculated with DARKSUSY for the selected DM candidates.

One of the most promising ways to observationally constrain the nature of DM is the detection of an anomalous spectral excess feature – a 'bump' – generated by the annihilating DM particles in the flux of electrons and positrons over the background produced by standard astrophysical systems. This possibility, predicted already by e.g. Ellis et al. (1988) and Kamionkowski & Turner (1991), has recently received great attention from the scientific community after the release of a number of sets of observations from the following: (i) *PAMELA*, an instrument for the detection of cosmic rays, with a particular focus on their antimatter component, attached to an Earth-orbiting satellite; (ii) *ATIC*, a balloon-borne experiment to measure the energy and composition of cosmic rays; (iii) *Polar Patrol Balloon* (*PPB*) with the *Balloon-borne Electron Telescope with Scintillating fibres* (*BETS*) imaging calorimeter, for the observations of cosmic ray electrons; and (iv) *Fermi*-LAT, a low Earth orbit space telescope used to perform gamma-ray observations (for a description of the aforementioned experiments, see e.g. Chang et al. 2008; Torii et al. 2008; Abdo et al. 2009; Adriani et al. 2009; Grasso et al. 2009).

The results from *PAMELA* showed an excess of positrons over the expected background generated by interactions between cosmic ray nuclei and interstellar matter in the energy range between 10 and 100 GeV. Complementary results by *ATIC* reported a sharp excess in the electron + positron flux in the energy range between 300 and 800 GeV, confirmed by similar results from *PPB-BETS*. Among the scenarios proposed to explain such deviations from the standard cosmic ray secondary positron model, the one that invokes DM particles that either decay or annihilate has received large attention and has been investigated by an enormous amount of publications (see e.g. Profumo 2008 for a comprehensive, but not exhaustive, list of references).

The later observations by *Fermi*-LAT, however, changed the scenario again. The LAT, as mentioned earlier, is a gamma-ray detector based on pair production and therefore, as it was pointed out in the early stages of its construction (e.g. Moiseev, Ormes & Moskalenko 2008), it can also act as a direct detector for high-energy electrons and positrons – assuming that an efficient way is found to separate them from other cosmic ray species, in particular from protons. Therefore, *Fermi*-LAT represents a very powerful instrument to probe the nature of DM since it can observe both the gamma-rays and the high-energy leptons hypothetically produced by decaying or annihilating DM particles.

The results published by the *Fermi*-LAT collaboration do not confirm the sharp feature in the $e^+ + e^-$ energy spectrum above the background as reported by *ATIC*; however, the spectrum appears to be significantly harder than previously believed and therefore either the electron spectrum at the source is harder or there is a further component previously not taken into account between 100 GeV and 1 TeV (Grasso et al. 2009). The absence of the *ATIC* feature was confirmed by the HESS atmospheric Cherenkov telescope (Aharonian et al. 2009). Below 1 TeV, the spectrum measured by HESS is in agreement with that of *Fermi*-LAT, while above that energy (a range not probed by *Fermi*-LAT) a significant spectral steepening was reported.

The mass $m_{\rm DM}$ of the annihilating or decaying DM candidate naturally represents a cut-off scale of the $e^{\pm}$ spectrum; therefore, the absence of a clear feature in the $e^+ + e^-$ energy spectrum from *Fermi*-LAT 'cooled down' the enthusiasm about the DM hypothesis. On the other hand, including known pulsars as sources of relativistically accelerated electrons and positrons allows us to explain consistently both the *PAMELA* and the *Fermi*-LAT data, making this the most likely scenario (e.g. Profumo 2008; di Bernardo et al. 2011). Moreover, DM particles with a large annihilation cross-section into leptons and a few TeV mass, such as those needed to explain the *PAMELA* and *Fermi* + HESS cosmic ray excesses in terms of DM, are ruled out either by the constraints imposed by the isotropic galactic diffuse gamma-ray emission (Abdo et al. 2010c) or by the observed optical depth of the Universe (Cirelli et al. 2009b). More recently, *Fermi* observations made it possible to put tighter constraints on high-mass DM candidates either by the absence of DM signals in the Milky Way satellites (Ackermann et al. 2011) or by a detailed analysis of the Galactic Centre region and diffuse galactic emissions (Porter, Johnson & Graham 2011).

Nevertheless, a DM particle with mass $100\,{\rm GeV} < m_{\rm DM} < 2\,{\rm TeV}$ that decays or annihilates dominantly in leptonic channels can still explain the positron excess observed by *PAMELA* and the energy spectrum measured by *Fermi*-LAT.

The direct detection of WIMPs through elastic collision with the nuclei at terrestrial targets, originally proposed by Goodman &

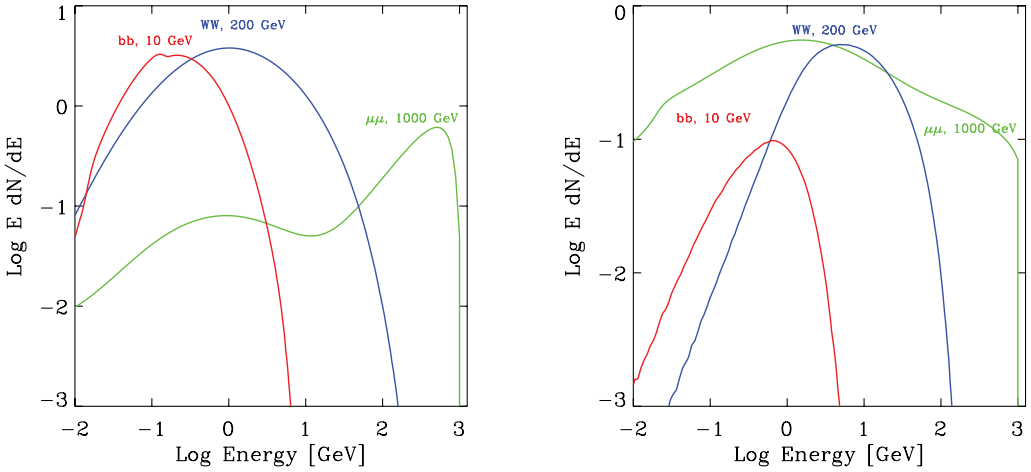

Figure 1. DM annihilation spectra for electrons + positrons (left-hand panel) and photons (right-hand panel).

Witten (1985), has been recently tested by experiments looking for anomalies possibly compatible with a DM signal. Stringent limits on the elastic WIMP-nucleon cross-section has been given by a number of experiments, such as CDMS-II (CDMS II Collaboration 2010), EDELWEISS-II (Armengaud et al. 2010) and XENON100 (Aprile et al. 2011). Note also that CoGeNT (Aalseth et al. 2011b) and DAMA/NaI (Bernabei et al. 2004) and DAMA/LIBRA (Bernabei et al. 2008) collaborations have observed an annual modulation signal, and the modulation signal phase matches well with the expected annual signal of WIMPS (Bernabei et al. 2010). However, the annual modulation claim has not been verified by any other experiments, especially the null results from CDMS, XENON10 and XENON100 data. In particular, the CDMS data (CDMS II Collaboration 2010) have reported two signal events against an expected background of 0.6 ± 0.1 events, but due to low statistics this result has not provided yet sufficient evidence for the DM detection. The analysis of the direct detection data are compatible with a light WIMP ($m_{\rm DM} \sim 10\,{\rm GeV}$) with strong coupling with quarks.

Note that this mass range has already been considered for potential imprints on CMB anisotropies by Galli et al. (2011) and Hütsi et al. (2011), who find stringent constraints on light DM particles (albeit their analysis has primarily focused on leptonic annihilation channels).

For our selection of three candidates from among the most promising DM candidates, we follow the criteria used in Evoli et al. (2011; see also Linden, Profumo & Anderson 2010 for a similar approach) and study the following: (i) a 10-GeV bino-like neutralino to test the case of hadronic channels; (ii) a heavy DM candidate of rest mass 1 TeV that pair annihilates into muons and gives as a result a hard energy spectrum in agreement with the *PAMELA* and *Fermi*-LAT observations; and (iii) an intermediate-mass 200 GeV wino-like neutralino with a pair annihilation into W^+W^- pairs and the consequent production of electrons and positrons (see Fig. 1).

3 METHOD

We start by introducing the new physics introduced in MEDEA2 with respect to the previous version of MEDEA used in VEF10. With such updates, described below, the new code is capable of following the energy cascade of a distribution of initial particles (electrons, positrons and/or photons) in a wider redshift range ($10 < z < 1000$) and for particle energies up to a few TeV, since at higher energies new interactions not included in the current version of the code could become important. In Table 1 we provide for clarity a succinct comparison between the two code versions.

Table 1. Comparison between the main features of MEDEA1 and MEDEA2.

Input	MEDEA1	MEDEA2
Primary e^-	√	√
Primary e^+	×	√
Primary γ	×	√
Single particle	√	√
Particle distribution	×	√
Redshift range	$10 < z < 50$	$10 < z < 1000$

For every primary particle and for the secondary ones produced in the shower, the algorithm calculates the mean free paths for the relevant interaction channels, assigning them an interaction probability $p_{\rm i} = \lambda_{\rm total}/\lambda_{\rm i}$ (where $\lambda_{\rm i}$ is the mean free path associated with the considered process and $\lambda_{\rm total}$ is the sum of all the possible mean free paths) and selecting one by a random number generator. The number of particles that the code has to follow naturally rises as more and more interactions take place in the process of energy degradation of the primaries. To lower the computational burden of this numerical approach, we set a number of energy thresholds over or under which we make some well-motivated simplifying assumption for the energy depositions, as described later in this section.

For each assumed primary energy distribution (which can be obtained for example from an input DM spectrum as we explain in Section 3.4) $f_{\rm in}(E_{\rm e^-}, E_{\rm e^+}, E_\gamma)$, we set the values of the two free parameters in our calculation – gas ionized fraction ($x_{\rm e}$) and redshift (z) – and for each set of values perform 100 Monte Carlo realizations, i.e. numerically follow the secondary energy cascade by repeated random sampling of the probability interactions. As shown in VF08, performing 100 realization per parameter choice allows us to have highly consistent results without any substantial bias due to the random nature of the computation, with an achieved convergence better than 1 per cent. Throughout our work, we define $x_{\rm e} \equiv n({\rm H}^+)/n({\rm H}) \equiv n({\rm He}^+)/n({\rm He})$ and we set the helium fraction by mass to be $f_{\rm HE} = 0.28$ in agreement with the 7-year *Wilkinson Microwave Anisotropy Probe* (*WMAP*7) data analysis (Larson et al. 2011).

In this section, we will review the physics related to the energy depositions from electrons, positrons and photons into the IGM.

While in the case of electrons, the processes are similar to the one described in VEF10, albeit with some crucial improvements and extensions at higher energies, the treatment of positrons and photons is instead entirely new.

3.1 Electrons

MEDEA2 follows in detail the fate of free electrons with a broad range of velocities by calculating the energy cascade that originates from the interactions with the surrounding gas. We find that the interaction probabilities of free electrons in the IGM depend largely on their velocity. When the kinetic energy is equivalent or higher than the electron rest mass (∼511 keV), IC dominates and bremsstrahlung is non-negligible (but only at high redshift), while at lower energies the most relevant processes are the following: H, He, He I collisional ionizations; H, He collisional excitations; and collisions with thermal electrons. Although there are these two obvious regimes, the code covers all the processes in the entire energy range for greater accuracy.

In the following, we describe the electron interactions implemented in the code.

3.1.1 Collisions with atoms

When a free electron collides with an atom, it can either set it to an excited state or ionize it if the kinetic energy $E_{\rm in}$ is higher than 10.2 or 13.6 eV, respectively.

When a free electron collisionally ionizes an H or He atom, a new free electron is generated, which has to be followed by the code. The energy distribution of these secondaries is treated as in VF08, while the cross-sections for the collisional ionization of H, He, He+ are taken from Kim & Rudd (1994), Shah, Elliott & Gilbody (1987) and Shah et al. (1988). When any of the electrons is degraded to energies below 10.2 eV, we assume that it thermalizes with the gas depositing its remaining energy as heat since no other relevant process can take place. This assumption stands for a gas with a temperature below 10^4 K.

If a collisional excitation on an atom takes place, the colliding free electron loses part of its energy, which is converted into photons emitted by the excited atoms returning to the ground state on a short time-scale. Our code follows these individual photons since they can interact further with gas. If their energy, on the other hand, is lower than 10.2 eV, we assume that no further interaction takes place. Such low-energy photons are mainly generated by transitions to/from the 2s level of H I, either by direct collisional excitations to 2s followed by the two-photon forbidden transition 2s–1s or by indirect cascades from $n \geq 3$ states which happen preferentially through the 2s level rather than through 2p (see e.g. Hirata 2006; Chuzhoy & Shapiro 2007). The collisional excitation cross-sections of H and He are from Stone, Kim & Desclaux (2002), while those to the 2s level of H are from Bransden & Noble (1976).

3.1.2 Coulomb scattering

Electron–electron collisional cross-section resulting in an energy loss $\Delta E_{\rm in}$ is given by

$$\sigma_{\rm ee} = 40\pi e^4 \ln\Lambda \left(\frac{0.05}{f}\right) E_{\rm in}^{-2}\,{\rm cm}^2, \tag{1}$$

where the Coulomb logarithm $\ln\Lambda = \ln(4E_{\rm in}/\zeta_{\rm e})$, with $\zeta_{\rm e} = 7.40 \times 10^{-11}\,(n_{\rm e}/{\rm cm}^{-3})$ eV and $f = \Delta E_{\rm in}/E_{\rm in} = 0.05$ is chosen to account for the discrete nature of the calculation (Shull & van Steenberg 1985; VF08; Furlanetto & Stoever 2010). The cross-section for Coulomb collisions between electrons is from Spitzer & Scott (1969).

After a Coulomb interaction, part of the kinetic energy is transferred elastically to the upscattered IGM thermal electrons whose fate will be consequently followed by MEDEA2.

3.1.3 Recombinations

The cross-section for hydrogen recombination is

$$\sigma_{\rm r}(\nu, n) \approx 3 \times 10^{10} \frac{g_{\rm fb}}{\nu n^3 v_{\rm e}^2}\ {\rm cm}^2, \tag{2}$$

where ν is the emitted radiation frequency, $g_{\rm fb} \sim 1$ is the Gaunt factor Karzas & Latter (1961), $v_{\rm e}$ is the electron velocity and n is the level at which the electron recombines. We find that this process is largely negligible relative to the other interactions.

3.1.4 bremsstrahlung

When an electron enters the field of a proton, ionized He atom or neutral H and He atoms, it is decelerated and emits a continuum photon. This process, known as free–free interaction or bremsstrahlung, is intrinsically dependent on a number of parameters and conditions, and its exact cross-section can be derived by the methods of quantum electrodynamics. However, a semiclassical approach under some reasonable assumptions and simplifications can lead to approximated cross-sections. A review of the experimental and theoretical results and of the different approximated cross-sections can be found in Koch & Motz (1959) and Blumenthal & Gould (1970).

In our calculations, bremsstrahlung is generally negligible as shown in VEF10, and only for very high energies $E_{\rm in} \geq 10^{11}$ eV the cross-section becomes comparable to those of the other processes. At these energies, however, IC is largely dominant.

3.1.5 Inverse Compton

When electron energies become relativistic, IC with CMB photons becomes by far dominant. To understand why, we first introduce briefly the physics of this particular process. The following is the IC angle averaged cross-section in ${\rm cm}^{-2}\,{\rm eV}^{-1}$:

$$\sigma_{\rm KN}\left(E_{\rm in}^{\gamma}, E_{\rm fin}^{\gamma}, \gamma_{\rm e}\right) = \frac{3\sigma_{\rm T}}{4{\gamma_{\rm e}}^2 E_{\rm in}^{\gamma}} G(q, \eta). \tag{3}$$

We denote here by $E_{\rm in}^{\gamma}$, $E_{\rm fin}^{\gamma}$ and $\gamma_{\rm e}$ the energy of the incoming and outgoing photon and the Lorentz factor of the incoming electron, respectively. $\sigma_{\rm T} = 8\pi {r_0}^2/3$ is the Thomson cross-section, while the function $G(q, \eta)$ is given by

$$G(q, \eta) = 2q\ln q + (1 + 2q)(1 - q) + 2\eta q(1 - q), \tag{4}$$

$$q = \frac{E_{\rm fin}^{\gamma}}{\Gamma\left(\gamma_{\rm e} m_{\rm e} c^2 - E_{\rm fin}^{\gamma}\right)}, \quad \Gamma = \frac{4E_{\rm in}^{\gamma}\gamma_{\rm e}}{m_{\rm e}c^2}, \quad \eta = \frac{E_{\rm in}^{\gamma} E_{\rm fin}^{\gamma}}{\left(m_{\rm e}c^2\right)^2}. \tag{5}$$

The energy distribution of the scattered photons is

$$\frac{{\rm d}N_{\gamma,{\rm E}_{\rm in}^{\gamma}}}{{\rm d}t\,{\rm d}E_{\rm fin}^{\gamma}} = \frac{2\pi {r_0}^2 c}{{\gamma_{\rm e}}^2} \frac{n\left(E_{\rm in}^{\gamma}\right){\rm d}E_{\rm in}^{\gamma}}{E_{\rm in}^{\gamma}} G(q, \eta) = c\sigma_{\rm KN} n\left(E_{\rm in}^{\gamma}\right){\rm d}\,E_{\rm in}^{\gamma}. \tag{6}$$

The only assumption for the validity of these equations is that $\gamma_e \gg 1$, i.e. that the electron is relativistic. If the energy of the incoming photon in the rest frame of the electron $E_{in}^{\gamma\,*} = \gamma_e E_{in}^{\gamma}(1-\beta\cos\theta) \ll m_e c^2$, we are in the Thomson limit; therefore $\Gamma \ll 1$ and the last term in $G(q,\eta)$ becomes negligible. The opposite case $E_{in}^{\gamma\,*} \gg m_e c^2$ is the extreme Klein–Nishina limit. If we consider a CMB photon at $z \sim 10$ ($E_{in}^{\gamma} \sim 2.35 \times 10^{-3}$ eV) and electron energies up to 1 TeV ($\gamma_e \sim 10^6$), we are still well within the Thomson limit; this limit is not valid anymore at high redshift when the full Klein–Nishina cross-section needs to be used.

Kinematic requirements set a lower and upper limit on the energy of the upscattered CMB photon (see e.g. Blumenthal & Gould 1970; Petruk 2009):

$$E_{fin(min)}^{\gamma} = E_{in}^{\gamma}, \quad E_{fin(max)}^{\gamma} = 4\gamma_e^2 E_{in}^{\gamma}. \tag{7}$$

For our purposes, we consider $\sigma_{KN}(E_{in}^{\gamma}, E_{fin}^{\gamma}, \gamma_e)$ which is given in $cm^2\,eV^{-1}$: from this quantity, we can derive the total IC cross-section for an electron and a photon with assigned initial energies by integrating equation (3) on the energy of the outgoing photon:

$$\sigma_{IC}\left(E_{in}^{\gamma}, \gamma_e\right) = \int_{E_{in}^{\gamma}}^{4\gamma_e^2 E_{in}^{\gamma}} \mathrm{d}E_{fin}^{\gamma} \frac{3\sigma_T}{4\gamma_e^2 E_{in}^{\gamma}} G\left(E_{fin}^{\gamma}\right). \tag{8}$$

To derive the probability for a given high-energy electron to scatter off CMB photons described by the distribution $n(E_{in}^{\gamma})$, we must calculate the mean free path for IC:

$$\lambda_{IC}(\gamma_e) = \frac{1}{\int \mathrm{d}E_{in}^{\gamma} n(E_{in}^{\gamma}) \sigma_{IC}(E_{in}^{\gamma}, \gamma_e)}. \tag{9}$$

In order to reduce the computational time, we calculate it in the Thomson limit, which is a good approximation in most of our redshift range:

$$\lambda_{IC} = \frac{1}{\sigma_T \int \mathrm{d}E_{in}^{\gamma} n\left(E_{in}^{\gamma}\right)}. \tag{10}$$

This quantity is dependent only on the initial electron energy if the isotropic initial photon energy distribution is known. Now we can calculate the relative probability of having IC and can follow the route of the electron into the IGM by Monte Carlo technique.

If the electron actually scatters off a CMB photon, we need to compute the energy kick to the photon and therefore the energy loss of the electron. To do so, we first determine the initial energy of photons, drawing it from their parent distribution. For this purpose, we use the rejection method to generate sampling photons from the distribution given by $n(E_{in}^{\gamma})\sigma_{IC}(E_{in}^{\gamma}, \gamma_e)$.

Once E_{in}^{γ} is determined, we similarly use the rejection method on the distribution $\sigma_{KN}(E_{in}^{\gamma}, E_{fin}^{\gamma}, \gamma_e)$ to infer the outgoing photon energy – and therefore the electron energy loss.

IC is by far the process that requires higher computational effort when following the cascade evolution since (i) it is the most probable interaction for a wide range of energies and (ii) energy loss by upscattering of CMB photons generally happens thorough a very high number of interactions that lower the electron kinetic energy by a small fraction at each step, accordingly to the limits given by equation (7). To reduce the computational time required to take into account the huge number of IC scatterings, the energies of the initial and the upscattered photons are tabulated functions of the redshift and of the electron velocity. We verify that with the adopted step size for the input redshift and velocity, the difference between the results obtained by interpolating the tabulated functions and the analytical solution obtained by solving equations (6) and (8) are below 1 per cent in the range $10 < z < 1000$ and $1 < \gamma_e < 10^6$.

In agreement with the analytical comparison between the IC energy loss time-scale and the Hubble time by Hansen & Haiman (2004), we find that the former is irrelevant for the energy loss process at energies:

$$E_{in} = \gamma_e m_e c^2 > \left(\frac{1+z}{21}\right)^{-1/2} \text{MeV}. \tag{11}$$

For this reason, in our simulation, we do not evaluate this process for electrons below this energy.

3.2 Positrons

The positrons injected in the IGM behave identically to electrons at high energies, as they lose their energy predominantly via IC scattering. At low energies, they can have similar kind of interactions with atoms (ionizations and excitations), however with different cross-section due to their different charge. Furthermore, the positrons can eventually form a positronium atom and annihilate in a very short time.

In Guessoum, Jean & Gillard (2005), the authors give a comprehensive review of the processes that a positron undergoes in the ISM and present updated positron interaction cross-sections with atomic hydrogen and helium. In particular, they calculate the cross-sections for excitation and ionization of atoms and positronium formation by charge exchange with atoms based either on theoretical calculations or recent experimental data (see Guessoum et al. 2005, for a list of references). In order to calculate the same processes in our simulation, we use the cross-section as a function of the positron energy that we take from their plots.

Moreover, the positrons can also annihilate with free electrons. The annihilation cross-section of a positron and an electron is described by (Heitler 1954)

$$\sigma_{ann} = \frac{\pi r_e^2}{\gamma+1}\left[\frac{\gamma^2+4\gamma+1}{\gamma^2-1}\log\left(\gamma+\sqrt{\gamma^2-1}\right) - \frac{\gamma+3}{\sqrt{\gamma^2-1}}\right], \tag{12}$$

where $\gamma = E_{in}/mc^2$ and r_e is the classical electron radius.

For collisional ionizations and excitations of atoms by positrons, we calculate the energies of the particle in the final state as described for the electron processes (see VF07). In the case of annihilation in the atom fields, since this process occurs only at low energy, we can neglect the relative velocity of the particle and assume that two photons are created, each with energy equal to the rest energy of the electron or positron (511 keV). On the contrary, for annihilation with free electrons, we calculate the energies of the emitted photons from the annihilation spectrum as given in Heitler (1954).

3.3 Photons

In the redshift and energy ranges we are considering in this work, the relevant interactions with matter for the photons are photoionization of atoms, Compton scattering on free electrons and pair production (both on atoms and free electrons). In particular, photoionization is considerably more important at lower energy (below 10^4 eV for $z \lesssim 100$), whereas the pair production is effective only at high redshift and for photon energies of $\gtrsim$TeV (see e.g. Zdziarski & Svensson 1989).

The photoionization cross-sections of neutral H and He (either neutral or ionized) are given by the fitting formulae from Verner

Table 2. Fit parameters for photo-ionization cross-sections in equation (13).

Ion	$E_{\rm th}$ (eV)	$E_{\rm max}$ (eV)	E_0 (eV)	σ_0 ($\times 10^{-18}$ cm^2)	y_α	P	$y_{\rm w}$	y_0	y_1
H I	1.360e+1	5.000e+4	4.298e−1	5.475e+4	3.288e+1	2.963e+0	0.000e+0	0.000e+0	0.000e+0
He I	2.459e+1	5.000e+4	1.361e+1	9.492e+2	1.469e+0	3.188e+0	2.039e+0	4.434e−1	2.136e+0
He II	5.442e+1	5.000e+4	1.720e+0	1.369e+4	3.288e+1	2.693e+0	0.000e+0	0.000e+0	0.000e+0

et al. (1996):

$$\sigma_{\rm ph}(E) = \sigma_0 F(y), \quad x = \frac{E}{E_0} - y_0, \quad y = \sqrt{x^2 + y_1^2},$$
$$F(y) = \left[(x-1)^2 + y_{\rm w}^2\right] y^{0.5P-5.5} \left(1 + \sqrt{y/y_\alpha}\right)^{-P}, \tag{13}$$

where E is photon energy in eV, $E_{\rm th}$ is the energy threshold for the process to be energetically possible and σ_0, E_0, $y_{\rm w}$, y_α, y_0, y_1 and P are the fit parameters whose value is reported in Table 2. Above the threshold, the energy carried off by the outgoing electron represents the balance between the energy supplied by the photon and the binding energy of the scattering atom.

The Compton scattering of an energetic photon by a free electron, assuming unpolarized photons and unaligned electrons, can be obtained from the Klein–Nishina formula (Heitler 1954). We adopt in our code the total cross-section obtained in two different energy regimes, namely $E \lesssim m_{\rm e}$ and $E \gtrsim m_{\rm e}$, and we assume

$$\sigma_{\rm c} = \sigma_{\rm T} \begin{cases} \frac{1+2E_\gamma+1.2E_\gamma^2}{1+2E_\gamma^2} & E_\gamma < 1, \\ \frac{3}{8} E_\gamma^{-1}(1 + 2\log 2E_\gamma) & E_\gamma > 1, \end{cases} \tag{14}$$

where E_γ is the photon energy expressed in terms of the electron mass. Note that at high energy ($E \gg 13.6$ eV), a photon is not able to distinguish whether an electron is free or bound; hence in analogy with Chen & Kamionkowski (2004), we treat all electrons as free for the Compton processes. To sample the final energy of the upscattered photon, we use the rejection method as described in the reference guide of the GEANT4 manual (Geant4 Collaboration 2003). The kinetic energy of the recoil electron is the energy lost by the photon during the interaction.

The pair production cross-sections are the same as in Slatyer et al. (2009). We adopt cross-sections for pair production on ionized H, free electrons and singly ionized He calculated in the Born approximation by Motz, Olsen & Koch (1969) with the modifications suggested by Joseph & Rohrlich (1958) for pair production off electrons.

Therefore, for ionized atoms (He II, He III and H II), we adopt

$$\sigma_{\rm pp,i} = \alpha r_{\rm e}^2 \left[\frac{28}{9}\ln(2E_\gamma) - \frac{218}{27}\right], \tag{15}$$

and for free electrons

$$\sigma_{\rm pp,e} = \alpha r_{\rm e}^2 \left[\frac{28}{9}\ln(2E_\gamma) - \frac{100}{9}\right], \tag{16}$$

where α is the fine-structure constant.

For pair production on neutral hydrogen and helium, we refer to the cross-sections from Zdziarski & Svensson (1989):

$$\sigma_{\rm pp,H} = 5.4\alpha r_{\rm e}^2 \ln\frac{513E_\gamma}{E_\gamma + 825}, \tag{17}$$

$$\sigma_{\rm pp,He} = 8.76\alpha r_{\rm e}^2 \ln\frac{513E_\gamma}{E_\gamma + 825}. \tag{18}$$

Also, for this process, we have implemented in MEDEA the algorithm described in the GEANT4 manual to calculate the kinetic energies of the electron and the positron in the final state.

We also take into account photon–photon pair production on the CMB radiation. In our treatment, photons with energy above the threshold,

$$E_{\rm th} \sim 2.6 \times 10^{11} \left(\frac{\epsilon_{\rm CMB}}{\rm eV}\right)^{-1} \text{ eV}, \tag{19}$$

(see e.g. Ferrigno, Blasi & de Marco 2005) generate a pair, since over $E_{\rm th}$ this process becomes highly dominant.

Finally, as discussed in many works (Zdziarski & Svensson 1989; Ullio et al. 2002; Chen & Kamionkowski 2004; Slatyer et al. 2009), the Universe is optically thin to energetic ($E \gtrsim 10^4$ eV) photons produced at redshift $z \lesssim 100$, which therefore contribute to the X-ray and gamma-ray extragalactic background (EGB). We account for this by taking that the photon free-streaming probability is inversely proportional to the Hubble radius, i.e. $p_{\rm f} = \lambda_{\rm total}/\lambda_{\rm H}$, and comparing it to the probabilities of the aforementioned processes. Due to cosmic expansion, the Hubble radius increases with time, $H(z)/c \propto (1+z)^{-3/2}$, whereas the mean free path of a specific process (if the cross-section is roughly constant with energy) is inversely proportional to the density. The interaction probability is then $\propto (1+z)^{-3/2}$, and we can safely assume that non-interacting photons at a given cosmic time will have an even smaller chance to interact in a later evolutionary phase.

3.4 DM-generated input spectra

A specific feature of MEDEA2, already mentioned in Section 1, is that it can follow the energy cascade of any arbitrary number of particles (electrons, positrons or photons) with different initial energies. Therefore, among its many possible applications, MEDEA2 is the ideal tool to study – as long as an initial energy spectrum can be assigned in input to the code – the energy deposition into the IGM from both DM decays and annihilations, since they produce, among the other particles, e^-/e^+ showers and photons.

In this work we focus on some of the most promising models for annihilating DM. The initial input spectrum, describing the annihilation product particles' energy distribution, is evaluated for the DM models by calling a specific routine of the DARKSUSY library. Then MEDEA2 generates the primary particles with a random sampling of the DM annihilation spectrum until the total energy of the extracted particles is equal to the energy integral of the DM spectrum. This ensemble of particles is used for the Monte Carlo realization of the particle cascade. Such procedure is repeated for photons, electrons and positrons. Note though that electrons and positrons from DM annihilation have the same distribution; however, due to the random sampling used to extract the primary particle energies, the initial realizations will slightly differ.

In Fig. 2, we show the histogram of the calculated electron energies by our code using the annihilation spectrum of the 200-GeV wino candidate as input distribution function. The histogram has been obtained averaging over 100 different realizations of the initial configuration. By comparing the histogram with the DM spectrum, we conclude that the particle energies calculated with the described procedure correctly sample the adopted distribution.

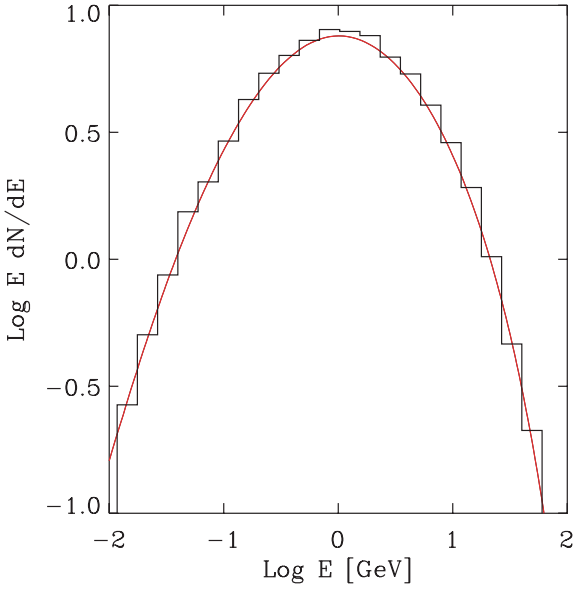

Figure 2. Comparison of the 200-GeV wino electron annihilation spectrum (red) with the normalized energy histogram (black) obtained with MEDEA2.

4 RESULTS

4.1 Mean free paths

Before we start the discussion on the energy deposition of primary particles, it is worth to comment on the relative importance of the processes that a single particle suffers in the IGM. In Fig. 3 we plot, for redshift $z = 10$, 100 and 1000, the inverse of the mean free paths of all the processes described in the previous section. Since this variable is directly proportional to the probability for that process to take place, this gives a clear indication of which process dominates at any considered redshift. For simplicity, in this plot, we assume that at each redshift the ionization fraction is the relic one.

From this plot it is evident that at high energies, electron and positron energy losses are dominated by IC, while at low energies ionization and excitation are more important than the other processes. In particular, for the assumed ionization fraction, positron annihilation does not play a significant role in dissipating the positron energy when it is in-flight. Therefore, annihilation is the final fate of a positron only after thermalization, and this motivates our assumption to consider the emitted photons as monoenergetic. Bremsstrahlung is important only in high-density regions and it becomes a subhorizon process only at very high redshift.

From the same plot we conclude that photons have lower probability to interact with the matter, and in some cases their total mean free path is larger than the Hubble radius at the considered redshift. At low energy, the photoionization of atoms instead becomes dominant. This is an important process since most of the IC upscattered photons are in the energy range and from this we can conclude that most of the energy lost by high-energy electrons and positrons is converted in low-energy electrons via IC and subsequent photoionization. Pair production is important only at high redshift, but its inclusion is fundamental to extend our calculations up to $z \sim 1000$.

4.2 Electron and positron energy deposition

We discuss here the fractional energy depositions for a single initial electron or positron injected into a partially ionized gas. We have already presented similar results in our previous work (VEF10), but the current treatment of the electron energy deposition is considerably refined, and the study of positrons is an entirely new feature of MEDEA2, which we will comment further in this section. Moreover, an analysis of these results is necessary to fully understand the final energy deposition outputs that arise from the DM annihilation spectra: these are nothing else than a combination of electrons, positrons and photons, which we determine using a given theoretical probability distribution and then use as input in MEDEA2.

In Fig. 4 we show the fractional deposition energy of a single electron (positron) for different initial energies. We consider which fraction of the initial electron energy is deposited into heat, Lyα photons, excitations, ionizations, photons with $E < 10.2$ eV and high-energy free-streaming photons. Hereafter, we will denote these fractions as $f_{\rm h}, f_\alpha, f_{\rm ion}, f_{\rm c}$ and $f_{\rm HE}$, respectively.

First we note that, even if similar in shape, $f_{\rm i}$ have different normalizations if we compare different initial energies. This behaviour holds at any redshift, and it is mainly due to the different impact of IC to dissipate the particle energy. In fact, most of the energy of the primary particle from its initial value down to the energy at which the IC became inefficient is lost by IC.

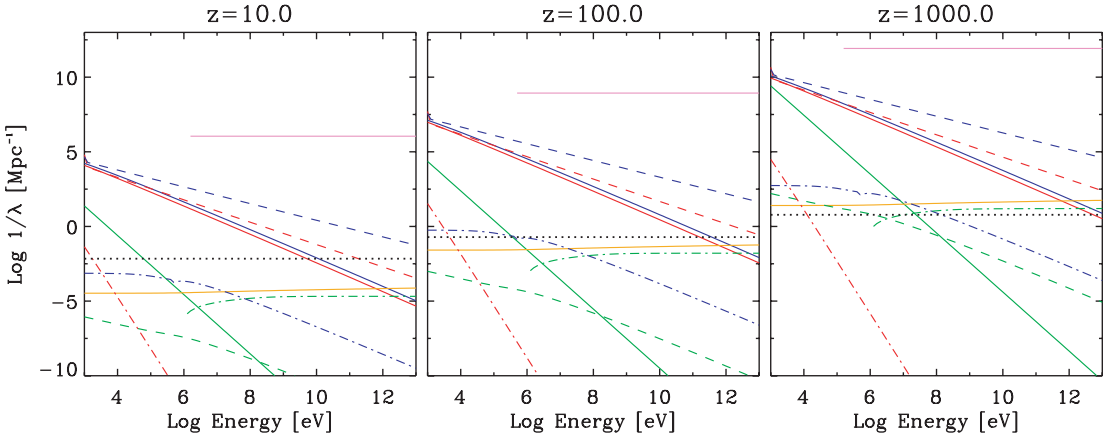

Figure 3. The inverse of the mean free paths of electrons, positrons and photons in the IGM. Electron interactions (solid): ionizations (red), excitations (blue), electron–electron encounters (green), bremsstrahlung (orange) and IC (violet). Positron interactions (dashed): ionizations (red), excitations (blue) and annihilations (green). Photon interactions (dot–dashed): photoionization (red), Compton (blue) and pair production (green). The dotted black line shows the inverse of the Hubble radius at the considered redshift.

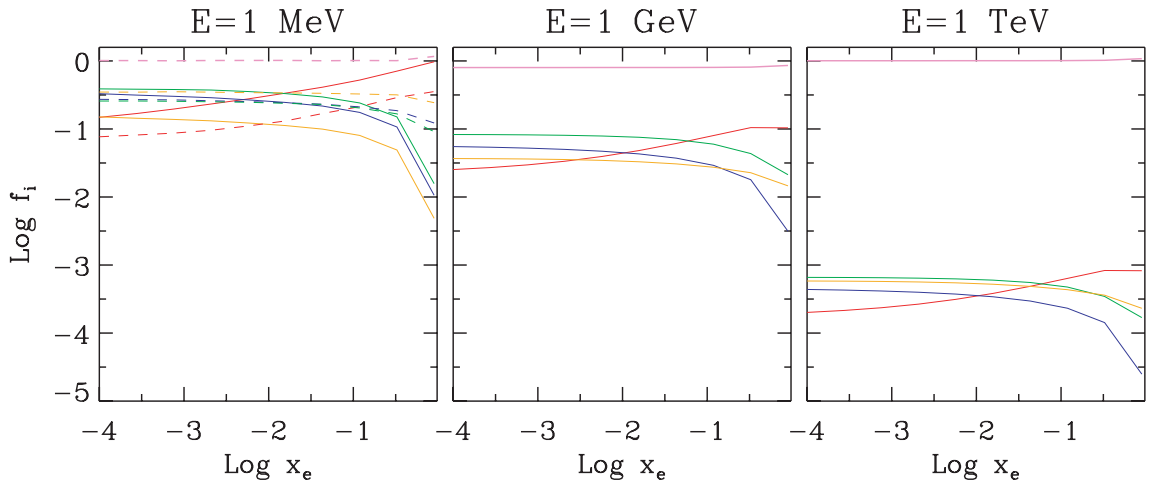

Figure 4. The energy deposition fractions for a single electron (solid line) and positron (dashed line) of different initial energies ($E = 10^6$, 10^9 and 10^{12} eV at $z = 10$). The curves represent the energy fraction that goes into gas heating ($f_{\rm h}$, red line), Lyα photons (f_α, green line), ionizations ($f_{\rm ion}$, blue line), photons with $E < 10.2$ eV ($f_{\rm c}$, orange line) and photons with higher energy that free stream to the observer ($f_{\rm HE}$, purple line). Note that in the middle and right-hand panels, the solid and dashed curves are indistinguishable.

The case of 1-MeV electrons is similar to what we had discussed already in VEF10. As the ionization fraction increases, the heating fraction becomes larger and the fraction of energy that goes into ionizations or low-energy and Lyα photons decreases. In fact, the probability for ionizations and excitations is proportional to the number of neutral atoms, and at high-ionization fractions, it becomes negligible. In this case, however, the low-energy photons are a smaller fraction of the total energy since they are only produced by atom ionizations and excitations. This is not true anymore if we increase either the initial electron energy or the redshift of the calculation: in these conditions, IC gives a significant contribution to the energy losses producing many low-energy photons that overcome in total integrated energy those produced by interactions with atoms.

The IC is also responsible for the production of a flattening of the Lyα photon fraction as the electron/positron initial energies increase. In these conditions in fact the Lyα fractional energy deposition is mainly composed of upscattered photons from IC with CMB photons, a process which does not depend on the ionized fraction.

The fractional energy depositions calculated in the case of single positrons in the same range of initial energies present in general a similar behaviour to the curves relative to electrons. This results can intuitively be expected since in the previous section we have shown that positrons undergo the same interactions with IGM atoms, with similar mean free paths. However, there are some significant differences which is worth mentioning. At $E_{\rm in} = 1$ MeV, the curves change significantly, and it is possible to note the effect of correctly assuming different cross-sections for electron and positron interaction with IGM atoms. An evident difference, however, derives from the fact that positrons – once their initial energy degrades below a certain threshold – inevitably annihilate, releasing two photons with total energy $E \gtrsim$ MeV. This can be seen easily for the 1-MeV positron case, for which the fraction of energy that is converted into photons can exceed unity. In particular, this happens at high values of the ionized fraction for which the interaction with atoms is suppressed and the annihilation happens in a relatively short on-flight time. The fractional energy depositions calculated for initial energy $E_{\rm in} = 1$ GeV, on the other hand, present a remarkably similar behaviour for electrons and positrons. This result can be anticipated

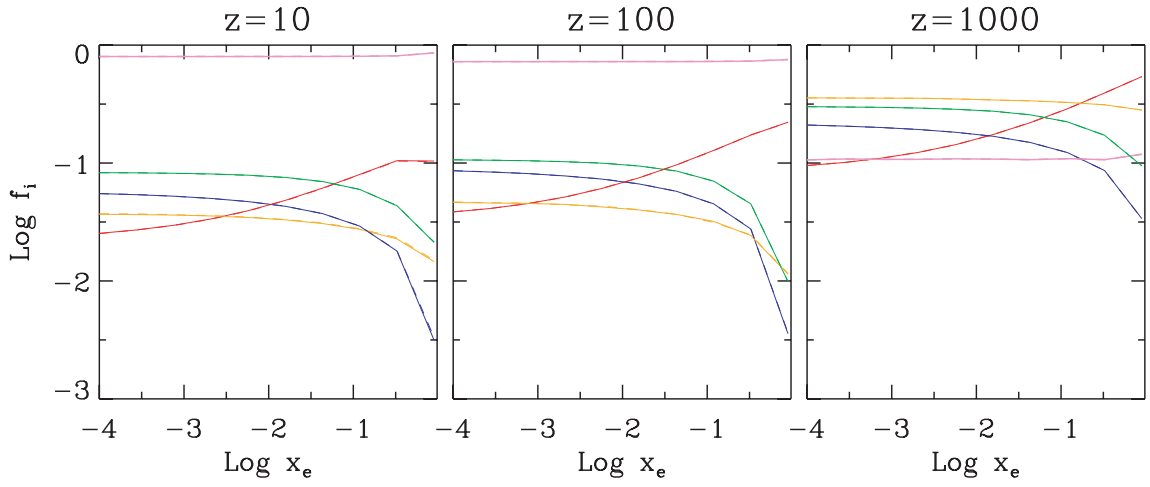

Figure 5. The energy deposition fractions for a single electron of $E = 10^9$ at different redshift $z = 10$, 100 and 1000. Colour codes are as in the previous figure.

by noticing that energetic leptons lose their energy mainly via IC, a process which is independent of the particle charge. The same can be said for the 1-TeV case where the positron and electron curves appear to be practically identical. It is interesting to note, however, the differences with respect to the results we found in our previous work (VEF10). In our new calculations, it is obvious that excitations and especially the production of low-energy photons become relatively more important: f_c remains the highest curve – apart from f_{HE} – up to $x_e \lesssim 0.1$, while in our previous calculations the same curve was up to one order of magnitude lower. The reason for this is the inclusion of Compton scattering: a highly relativistic lepton of 1 TeV will initially upscatter CMB photons to energies $\gtrsim$GeV until when its energy degrades substantially. These high-energy photons, however, can do Compton scattering and produce electrons in the right energy range to upscatter CMB photons to energies $1 \lesssim h\nu \lesssim 13.6$ eV, thus enhancing the relative importance of the aforementioned fractional energy deposition curves.

Comparing instead the 1-GeV case at different redshifts (Fig. 5), it is possible to note that the fractional energy depositions tend to increase at higher redshifts. This result can be easily explained if we consider that at these energies the upscattered IC photons are energetic enough to Compton scatter off the IGM gas and produce low-energy electrons. Since the energy of the upscattered CMB photons and the probability to have a Compton scattering all increase with redshift, there will be an enhanced production in the IGM of low-energy secondary electrons which deposit their kinetic energy into the gas more efficiently, hence the higher fractional energy depositions.

4.3 DM energy deposition

Finally, we assume specific DM initial energy spectra and discuss the calculated final outputs. In this case, the fractional energy depositions we plot are relative to the particle rest mass. It is worth noting that, by doing this, we also take into account the fraction of the initial energy released by the annihilations that goes into neutrinos and other non-interacting particles, which, for our purposes, is accounted as lost energy.

In Figs 6–8, we present the results of our calculations relative to the DM candidates introduced in Section 2. As expected, the fractional energy depositions for the considered DM candidates strongly depend on particle mass. In general, for increasing DM masses, the fractional energy deposition f_{HE} tends to become more important at the expense of the other f_i. This means that lower mass candidates would leave a stronger imprint on the ionization and thermal history of the IGM, and in principle they could be

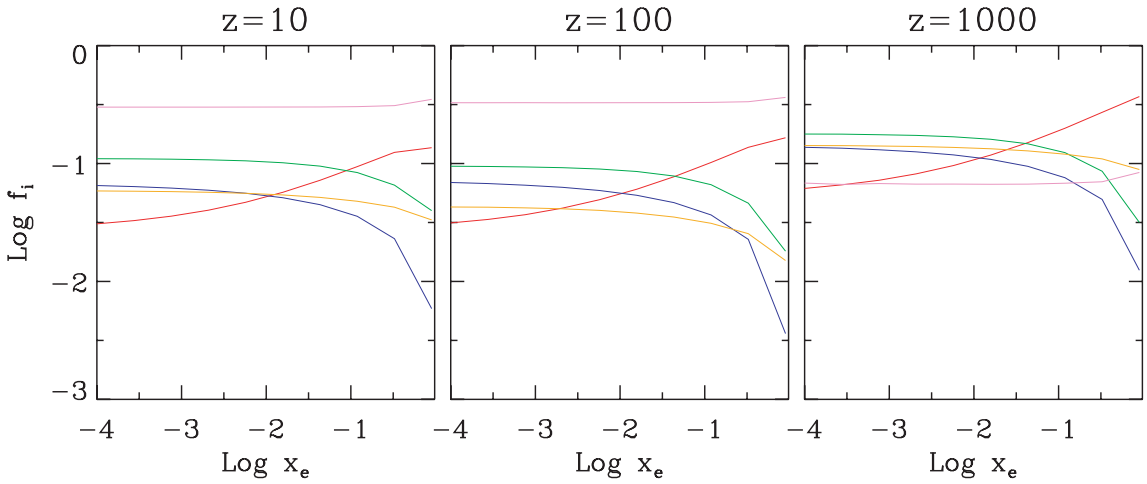

Figure 6. Fractional depositions from DM annihilation of a 10-GeV $b\bar{b}$ DM candidate. Line colours as in Fig. 4.

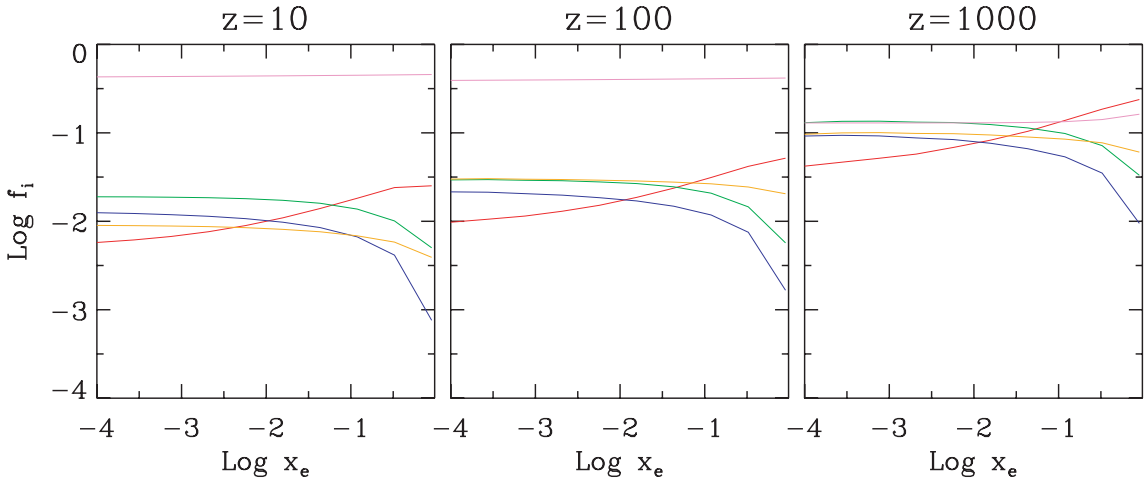

Figure 7. Fractional deposition from DM annihilation of a 200-GeV W^+W^- DM candidate.

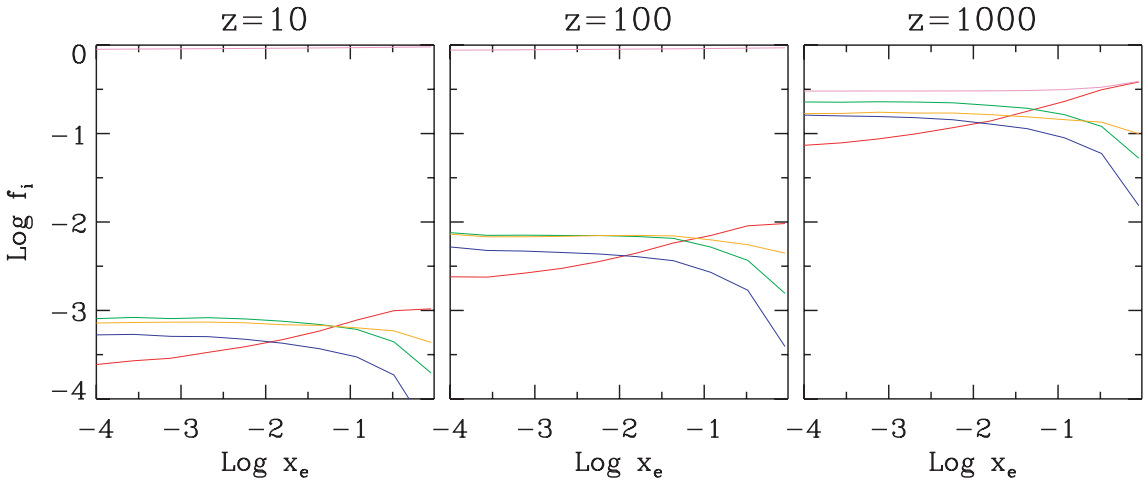

Figure 8. Fractional deposition from DM annihilation of a 1 TeV $\mu^+\mu^-$ DM candidate.

constrained more easily via e.g. H I 21-cm observations. On the other hand, heavier DM candidates produce more high-energy photons that free stream to the observer and therefore they can be better constrained via gamma-ray and X-ray observations.

The use of EGB measures to constrain DM properties recently gained popularity since the LAT instrument on board the *Fermi Gamma-ray Space Telescope* has provided new EGB data in the range 0.1–100 GeV (Abdo et al. 2010b). Immediately after, Abdo et al. (2010a) showed that the contribution of blazars to the EGB is non-dominant, and that new sources must be invoked to explain the observed fluxes. Recently, Cavadini, Salvaterra & Haardt (2011) proposed a model of the EGB based on the gamma-ray emission from blazars, non-beamed active galactic nuclei and star-forming galaxies. Their model leaves room for a possible contribution from annihilating DM, and a candidate particle with mass ∼0.5 TeV and cross-section $\langle\sigma v\rangle \sim 5 \times 10^{-26}$ cm^3 s^{-1} is shown to be in agreement with the data.

It is an interesting exercise to compare the fractional energy depositions calculated by MEDEA2 for a specific DM candidate with the depositions arising from a single particle with energy comparable with the DM rest mass. This gives a qualitative measure of the importance of using in input the proper primary spectral energy distributions for each DM candidate. To exemplify this point, we can compare the case of our most massive candidate (1 TeV, see Fig. 8) with that of a single 1-TeV electron (see Fig. 4), which is the ideal situation of a monochromatic spectrum in which all the DM-injected energy is converted into a single electron. We find that at redshift $z = 10$, the case in which the actual primary energy spectrum has been considered gives ∼2 times higher fractional energy depositions with respect to the monochromatic case, even taking into account that ∼30 per cent of the DM total released energy is lost in neutrinos. The relative importance of considering the actual spectrum depends on the shape of the annihilation spectrum itself, and increases dramatically for lower mass spectra.

At the same time, it is crucial to consider the discrete nature of the secondary products that arise from the primary energy spectrum, a requirement which is naturally met by the nature of our Monte Carlo calculation. Since most of the energy is quickly converted into (i) primary photons via the annihilation channel and (ii) secondary energetic photons via IC, it is especially important to treat them carefully. As mentioned earlier, for each particle, the code calculates the relevant interaction probabilities and compares them with the probability of non-interaction – i.e. free streaming – which is given by the inverse of the Hubble radius at the considered redshift. This treatment is especially important for energetic photons, since the mean free path of the allowed interaction channels are generally much larger than the Hubble radius, meaning that they will likely free stream to the observer since (even accounting for redshifting) they remain in the transparency window (see e.g. fig. 2 of Slatyer et al. 2009). A single energetic photon followed by the code will therefore most likely free stream and its energy counted as lost energy, i.e. not absorbed by the IGM. There is a non-negligible chance that interactions with the surrounding gas might happen, but in that case only a fraction (which is consistently computed by MEDEA2) of its initial energy will be deposited into the gas.

Most of these interactions always have a mean free path which is $\mathcal{O}(c/H(z))$; therefore, in principle, the interaction could occur at a lower redshift with respect to the production one. As a result, our model might overestimate the absorption fraction (i.e. the sum of all the f_i apart from the $f_{\rm HE}$) at higher redshift and underestimate it at lower redshift. However, a direct comparison with the results of Slatyer et al. (2009) in which the redshifting of photons has been properly taken into account shows that this approximation affects our predicted absorption fractions to a factor of <2. The advantage of our approach is, however, that it allows us to follow the fate of the low-energy tail of the particle cascade produced by primaries, and hence to predict the effective deposited energy which is transferred to the IGM as ionization and heating in detail. It has to be noted that any ionization fraction can be used as input parameter of the model, making it suitable to evaluate the impact of an exotic component to any prescribed cosmological ionization history.

4.4 Fitting formulae

In order to calculate the ionization fraction and temperature evolution of the IGM in the presence of DM annihilations, it is necessary to know which fraction of the injected energy contributes to ionization, heating and Lyα photons. As we have discussed in the previous sections, these functions depend on redshift (mainly due to IC energy losses) and on the ionization fraction of the medium. Therefore, in this section, we provide simple analytical fits of our numerical results that can be used in all the cases in which a full simulation of the evolution of single particles into the IGM at many different redshifts is not required.

Table 3. Model: $b\bar{b}$, 10 GeV.

f_i	A_0	A_1	A_2	B_0	B_1	B_2	C_0	C_1	C_2
f_h	−5.69e−01	−3.21e−01	1.29e−01	4.14e−01	−4.02e−02	1.15e−02	8.33e−01	2.16e−02	−3.02e−03
f_a	−8.08e−01	−4.80e−01	1.64e−01	−1.16e−01	3.80e−01	−9.23e−02	−3.04e−02	8.58e−01	−2.08e−01
$f_{ion,H}$	−7.70e−01	−4.54e−01	1.51e−01	2.91e−02	2.81e−01	−5.67e−02	−3.19e−01	8.74e−01	−1.81e−01
$f_{ion,He}$	−9.64e−01	−7.37e−01	1.78e−01	4.69e−01	−2.71e−01	5.96e−02	−2.24e−02	1.05e−01	−2.19e−03

Table 4. Model: W^+W^-, 200 GeV.

f_i	A_0	A_1	A_2	B_0	B_1	B_2	C_0	C_1	C_2
f_h	−1.37e+00	−3.14e−01	1.95e−01	3.57e−01	2.73e−02	−9.36e−03	8.60e−01	0.0	0.0
f_a	−1.77e+00	−3.24e−01	2.04e−01	2.85e−01	−2.70e−02	−4.09e−03	9.28e−01	−9.84e−02	−3.74e−03
f_{iH}	−1.71e+00	−3.58e−01	2.12e−01	3.31e−01	3.53e−02	−2.05e−02	4.68e−01	1.95e−01	−6.41e−02
f_{iHe}	−1.95e+00	−7.24e−01	2.88e−01	1.89e−01	−4.11e−02	1.41e−02	−6.49e−02	2.37e−01	−5.46e−02

Table 5. Model: $\mu^+\mu^-$, 1 TeV.

f_i	A_0	A_1	A_2	B_0	B_1	B_2	C_0	C_1	C_2
f_h	−3.22e+00	2.00e−02	3.10e−01	4.50e−01	−1.65e−01	4.50e−02	8.30e−01	2.50e−02	−5.00e−03
f_a	−3.86e+00	4.55e−01	1.95e−01	4.50e−01	−3.20e−01	8.00e−02	8.00e−01	−1.10e−01	2.00e−02
f_{iH}	−3.67e+00	2.55e−01	2.45e−01	5.80e−01	−3.30e−01	8.00e−02	6.00e−01	−5.00e−02	1.00e−02
f_{iHe}	−4.12e+00	1.20e−01	2.70e−01	4.90e−01	−2.65e−01	4.50e−02	1.40e−01	7.00e−02	−2.00e−02

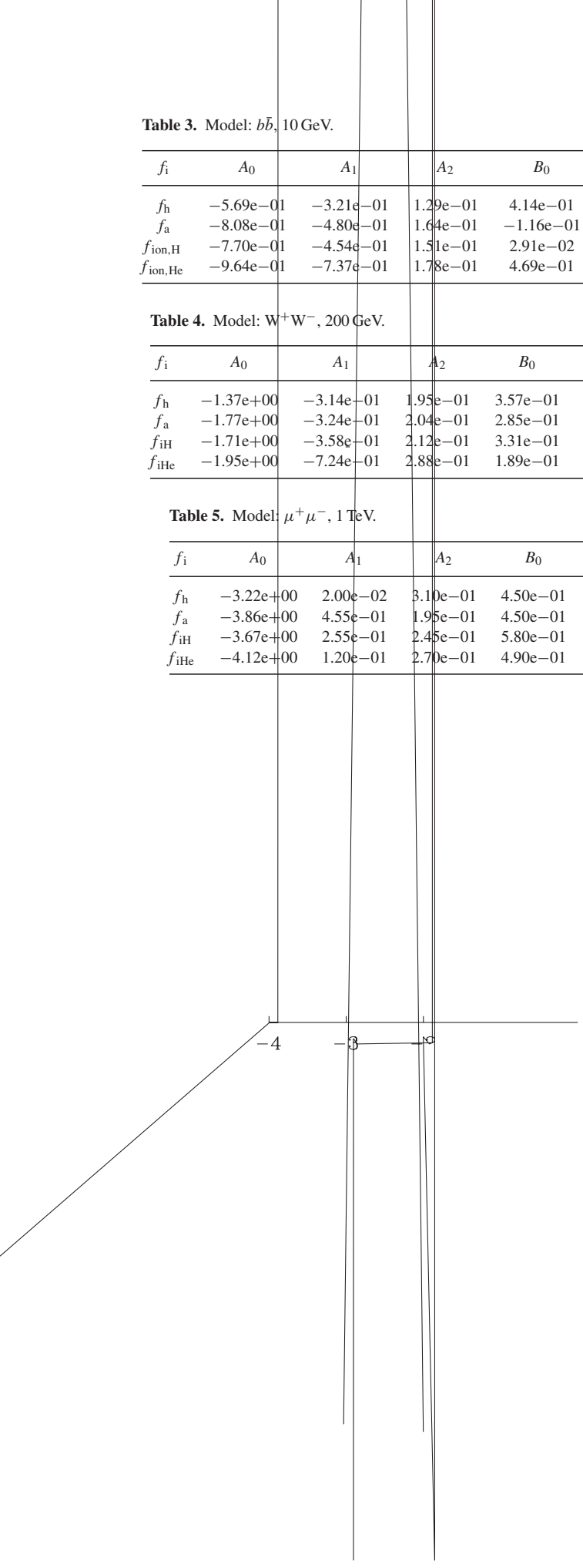

astrophysical environments characterized by their ionized fraction, baryonic density, H/He fraction and photon background. To perform our calculation we implemented in the code updated cross-sections for all the relevant interactions of electrons, positrons and photons with H and He atoms, free electrons and background CMB photons.

From a cosmological perspective, it is particularly interesting to consider the impact on the high-redshift ionization history of DM annihilation. In this scenario, DM may still contribute a non-negligible fraction of the measured free-electron optical depth.

To this aim, we have applied our model to study the energy deposition of DM annihilation products in the high-redshift IGM for three interesting DM models that have been proposed as possible candidates to explain the most recent observational results. For this specific application, the current version of the code can be safely applied in the redshift range $10 < z < 1000$.

We have found that the energy deposition strongly depends on the mass and on the annihilation spectrum of the DM particle. In particular, low-mass candidates are the favourite candidates to affect the high-z IGM properties.

The results presented here can be used for any astrophysical application in which it is necessary to deal with DM annihilation products and their interaction with the surrounding thermal gas. For this reason, we will periodically update tabulated results for the most interesting DM candidates at the URL http://wiki.arcetri.astro.it/bin/view/DAVID/MedeaCode.

Finally, we have also provided handy analytical fits to our numerical results that can be used to investigate the effects and detectability of the considered DM candidates at high-redshift IGM, e.g. via observations of the redshifted 21-cm emission.

ACKNOWLEDGMENTS

We thank T. Slatyer for constructive and open discussions and S. Baek and L. Maccione for helpful suggestions. CE acknowledges a visiting grant from SNS where part of this work has been carried out. NY acknowledges the financial support by the Grants-in-Aid for Young Scientists (S) 20674003 by the Japan Society for the Promotion of Science. Use of DEMOCRITOS/SISSA computer facilities are kindly acknowledged.

REFERENCES

Aalseth C. E. et al., 2011a, Phys. Rev. Lett., 106, 131301
Aalseth C. E. et al., 2011b, Phys. Rev. Lett., 107, 141301
Abdo A. A. et al., 2009, ApJ, 703, 1249
Abdo A. A. et al., 2010a, ApJ, 720, 435
Abdo A. A. et al., 2010b, Phys. Rev. Lett., 104, 101101
Abdo A. A. et al., 2010c, J. Cosmol. Astropart. Phys., 4, 14
Ackermann M. et al., 2011, Phys. Rev. Lett., 107, 241302
Adriani O. et al., 2009, Nucl. Phys. B Proc. Suppl., 188, 296
Aharonian F. et al., 2009, A&A, 508, 561
Aprile E. et al., 2011, Phys. Rev. Lett., 107, 131302
Armengaud E. et al. (EDELWEISS Collaboration), 2010, preprint (arXiv:1011.2319)
Bergström L., Edsjö J., Zaharijas G., 2009, Phys. Rev. Lett., 103, 031103
Bernabei R. et al., 2004, preprint (astro-ph/0405282)
Bernabei R. et al., 2008, European Phys. J. C, 56, 333
Bernabei R. et al., 2010, European Phys. J. C, 67, 39
Blumenthal G. R., Gould R. J., 1970, Rev. Modern Phys., 42, 237
Bowman J. D., Morales M. F., Hewitt J. N., 2005, BAAS, 37, 1217
Bransden B. H., Noble C. J., 1976, J. Phys. B At. Mol. Phys., 9, 1507
Cavadini M., Salvaterra R., Haardt F., 2011, preprint (arXiv:1105.4613)
CDMS II Collaboration, 2010, Sci, 327, 1619
Chang J. et al., 2008, Adv. Space Res., 42, 431
Chen X., Kamionkowski M., 2004, Phys. Rev. D, 70, 043502
Chuzhoy L., Shapiro P. R., 2007, ApJ, 655, 843
Ciafaloni P., Comelli D., Riotto A., Sala F., Strumia A., Urbano A., 2011, J. Cosmol. Astropart. Phys., 3, 19
Cirelli M., Kadastik M., Raidal M., Strumia A., 2009a, Nucl. Phys. B, 813, 1
Cirelli M., Iocco F., Panci P., 2009b, J. Cosmol. Astropart. Phys., 10, 9
di Bernardo G., Evoli C., Gaggero D., Grasso D., Maccione L., Mazziotta M. N., 2011, Astropart. Phys., 34, 528
Ellis J. R., Hagelin J. S., Nanopoulos D. V., Olive K. A., Srednicki M., 1984, Nucl. Phys. B, 238, 453
Ellis J., Flores R. A., Freese K., Ritz S., Seckel D., Silk J., 1988, Phys. Lett. B, 214, 403
Evoli C., Cholis I., Grasso D., Maccione L., Ullio P., 2011, preprint (arXiv:1108.0664)
Ferrigno C., Blasi P., de Marco D., 2005, Astropart. Phys., 23, 211
Fitzpatrick A. L., Hooper D., Zurek K. M., 2010, Phys. Rev. D, 81, 115005
Furlanetto S. R., Stoever S. J., 2010, MNRAS, 404, 1869
Furlanetto S. R., Oh S. P., Pierpaoli E., 2006, Phys. Rev. D, 74, 103502
Galli S., Iocco F., Bertone G., Melchiorri A., 2011, Phys. Rev. D, 84, 027302
Geant4 Collaboration, 2003, Nucl. Instrum. Methods Phys. Res. A, 506, 250
Goldberg H., 1983, Phys. Rev. Lett., 50, 1419
Gondolo P., Edsj

Spitzer L., Jr, Scott E. H., 1969, ApJ, 158, 161
Stone P. M., Kim Y. K., Desclaux J. P., 2002, J. Res. Natl. Inst. Standards Technol., 107, 327
Torii S. et al., 2008, preprint (arXiv:0809.0760)
Ullio P., Bergström L., Edsjö J., Lacey C., 2002, Phys. Rev. D, 66, 123502
Valdés M., Ferrara A., 2008, MNRAS, 387, L8 (VF08)
Valdés M., Ferrara A., Mapelli M., Ripamonti E., 2007, MNRAS, 377, 245
Valdés M., Evoli C., Ferrara A., 2010, MNRAS, 404, 1569 (VEF10)
Verner D. A., Ferland G. J., Korista K. T., Yakovlev D. G., 1996, ApJ, 465, 487
Wyithe J. S. B., Loeb A., Barnes D. G., 2005, ApJ, 634, 715
Zdziarski A. A., Svensson R., 1989, ApJ, 344, 551

This paper has been typeset from a TEX/LATEX file prepared by the author.